

# External scaffold of spherical immature poxvirus particles is made of protein trimers, forming a honeycomb lattice

Patricia Szajner,<sup>1</sup> Andrea S. Weisberg,<sup>1</sup> Jacob Lebowitz,<sup>2</sup> John Heuser,<sup>3</sup> and Bernard Moss<sup>1</sup>

<sup>1</sup>Laboratory of Viral Diseases, National Institute of Allergy and Infectious Diseases (NIAID), and <sup>2</sup>Division of Bioengineering and Physical Science, Office of Research Services, National Institutes of Health (NIH), Bethesda, MD 20892

<sup>3</sup>Department of Cell Biology, Washington University School of Medicine, St. Louis, MO 63110

**D**uring morphogenesis, poxviruses undergo a remarkable transition from spherical immature forms to brick-shaped infectious particles lacking helical or icosahedral symmetry. In this study, we show that the transitory honeycomb lattice coating the lipoprotein membrane of immature vaccinia virus particles is formed from trimers of a 62-kD protein encoded by the viral D13L gene. Deep-etch electron microscopy demonstrated that anti-D13 antibodies bound to the external protein coat and that lattice fragments were in affinity-purified D13 preparations. Soluble D13 appeared mostly

trimeric by gel electrophoresis and ultracentrifugation, which is consistent with structural requirements for a honeycomb. In the presence or absence of other virion proteins, a mutated D13 with one amino acid substitution formed stacks of membrane-unassociated flat sheets that closely resembled the curved honeycombs of immature virions except for the absence of pentagonal facets. A homologous domain that is present in D13 and capsid proteins of certain other lipid-containing viruses support the idea that the developmental stages of poxviruses reflect their evolution from an icosahedral ancestor.

## Introduction

Poxviruses are large, enveloped DNA viruses that replicate and assemble in the cytoplasm of infected cells (Moss, 2001). The structure of poxvirus virions is complex, and the outer surface, unlike that of most other viruses (<http://www.ncbi.nlm.nih.gov/ICTVdb/Ictv/ICTVindex.htm>), lacks helical or icosahedral symmetry. Immature virions (IVs), however, are completely enclosed by a honeycomb lattice (Heuser, 2005), the formation and fate of which are poorly understood. The first viral forms that can be recognized by EM in cells infected with vaccinia virus (VACV) and other poxviruses are cytoplasmic crescent-shaped membranes (Dales and Siminovitch, 1961; de Harven and Yohn, 1966). Initial EM images of thin sections suggested that a dense layer of radially oriented “spicules” covers the convex surface of these crescents, providing curvature and rigidity (de Harven and Yohn, 1966; Grimley et al., 1970; Dales et al., 1978). Subsequent grazing thin sections of crescents that were imaged by transmission EM (Mohandas and Dales, 1995) and recent deep-etch EM views of crescent surfaces (Heuser, 2005) demonstrated that the so-called spicules represent side

views of a honeycomb lattice that covers the entire exterior of crescents. Crescent membranes develop into spherical 300-nm diameter IVs that enclose DNA and core protein precursors while retaining the external honeycomb. However, during further steps of morphogenesis, IVs condense into infectious brick-shaped intracellular mature virions (IMVs) that no longer display the honeycomb lattice (Heuser, 2005). Evidently, the lattice has only a temporary “scaffolding” role during early morphogenesis and is lost during the shape transition.

The honeycomb lattice is not formed on the surface of viral membranes when cells are infected with VACV in the presence of the drug rifampicin (Moss et al., 1969; Grimley et al., 1970; Nagaya et al., 1970). Instead, irregular viral membranes surround masses that are composed of electron-dense material, forming structures called membrane-limited domains or rifampicin bodies. Upon removal of the drug, these irregular membranes rapidly acquire the characteristic curvature and honeycomb coating even in the absence of further protein synthesis (Moss et al., 1969). Thus, the viral membrane and scaffold need not associate coordinately, although they do during normal virogenesis. Several lines of evidence suggest that the 62-kD protein encoded by the D13L (VACWR118) gene is the target of rifampicin: (1) VACV mutations that confer resistance

Correspondence to Bernard Moss: [bmoess@nih.gov](mailto:bmoess@nih.gov)

Abbreviations used in this paper: 2-D, two dimensional; 3-D, three dimensional; IMV, intracellular mature virion; IV, immature virion; VACV, vaccinia virus.

to rifampicin map to the D13L gene (Tartaglia et al., 1986; Baldick and Moss, 1987); (2) repression of D13L expression blocks virus assembly and results in the formation of membrane-delimited masses of viroplasm that closely resemble those formed in the presence of rifampicin (Zhang and Moss, 1992); and (3) in the presence of rifampicin, D13 itself accumulates into large cytoplasmic masses, evidently because it is unable to associate with crescent and IV membranes (Miner and Hruby, 1989; Sodeik et al., 1994; Mohandas and Dales, 1995). In addition, early biochemical investigations suggest that an ~65-kD protein, which was subsequently found to be D13, is associated with immature viral membranes (Essani et al., 1982). These studies and others (Mohandas and Dales, 1995) suggested that this ~65-kD protein forms an outer layer on the convex side of the IV membrane. However, certain other reports disagreed and claimed instead that D13 is associated with the concave inner surface of the IV membrane (Sodeik et al., 1994; Vanslyke and Hruby, 1994).

This study resolves the previous disagreement by demonstrating conclusively that the D13 protein assembles on the exterior of the IV to form the curved honeycomb lattice, which is made mostly of hexagons and some pentagons. In addition, we show that a point mutation in the gene encoding D13 results in the formation of flat sheets that are not membrane associated and exclusively contain hexagons. The D13 protein was demonstrated to be homotrimeric like the proteins comprising the capsids of many icosahedral viruses. Moreover, homology between a domain of the D13 protein and capsid proteins covering the membranes of some DNA viruses (Iyer et al., 2001) suggests that poxvirus IVs correspond to the mature virions of such viruses. Thus, the morphogenesis of poxviruses may recapitulate their evolution from an ancestral icosahedral virus to a more complex form.

## Results

### Localization of D13 protein on the IV

Our first efforts to localize D13 involved EM imaging of standard thawed 70-nm cryosections of cells that were infected with VACV and immunodecorated with an antibody to a COOH-terminal peptide of D13 followed by the imaging of protein A conjugated to 10-nm gold. This procedure yielded many gold particles on IV membranes but few on mature virus particles (Fig. 1), as previously reported (Miner and Hruby, 1989; Sodeik et al., 1994; Mohandas and Dales, 1995). In such cryosections, some IVs appeared to have thick and blurry shells, whereas others appeared to be bounded by relatively sharp membranes (Fig. 1). We presumed that the blurred images were caused by different diameters of superimposed upper and lower surfaces of IV that had been cut near one of its poles rather than symmetrically on either side of the equator. In such blurry images, gold typically appeared to label the inner surface of the shell (Fig. 1). In contrast, gold grains appeared directly on or just outside of IV membranes that appeared to have sharp, thin shells (Fig. 1). To determine whether this pattern of labeling was epitope dependent, we constructed a replication-competent VACV (vV5D13) that expresses D13 with an NH<sub>2</sub>-

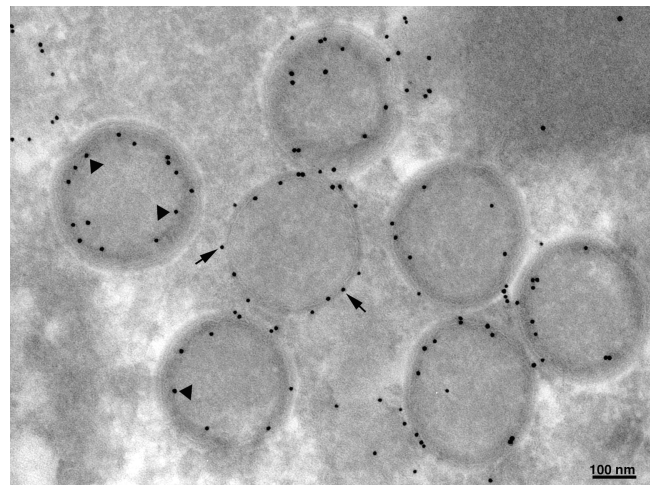


**Figure 1. Transmission EM images of immunogold-labeled IV.** Thawed cryosections of cells infected with VACV were labeled with antibody to the COOH-terminal peptide of D13 followed by protein A conjugated to 10-nm gold particles. Arrowheads point to gold particles that appear to line the concave inner surface of the shells of IVs; arrows point to gold particles that appear to be associated with the convex surface of an IV.

terminal V5 epitope tag. The same pattern of gold decoration was obtained with an antibody to this NH<sub>2</sub>-terminal epitope (unpublished data) as was found with the antibody to the COOH terminus.

The aforementioned ambiguity in localizing D13 by standard transmission EM is exactly what created earlier discrepancies in the literature (Sodeik et al., 1994; Vanslyke and Hruby, 1994; Mohandas and Dales, 1995). To obtain more definitive three-dimensional (3-D) information about the localization of D13 relative to the IV membrane, we examined antibody-decorated cryosections by deep-etch EM. To do this, cryosections were prepared and immunogold labeled as usual, but the sections were freeze dried and platinum replicated before EM viewing. This added step provided much clearer images of IVs and their external honeycomb lattices, which immediately revealed that gold particles label only the cut edges of IVs on the uppermost surfaces of cryosections (Fig. 2 A). Thus, the gold particles formed circular arrays around each IV exactly where it emerged from the section, regardless of how far from its equator it happened to be cut (Fig. 2, B and C). In Fig. 2, we show this with a monoclonal antibody to the V5 epitope that was appended to the NH<sub>2</sub> terminus of D13, but the same result was obtained with the aforementioned polyclonal antibody that targeted the COOH terminus of D13 itself (not depicted). One possible explanation for this result is that primary antibodies and/or protein A-gold conjugates are unable to penetrate into such cryosections as a result of simple size exclusion. Alternatively, specific D13 or V5 epitopes that the antibodies recognize may be masked on the surface of the assembled honeycomb and may only be exposed on its cut edge. In any case, the exclusive surface labeling clearly demonstrated why D13 appears to be on the inside of IV membranes that were sectioned near the upper pole and viewed by transmission EM.

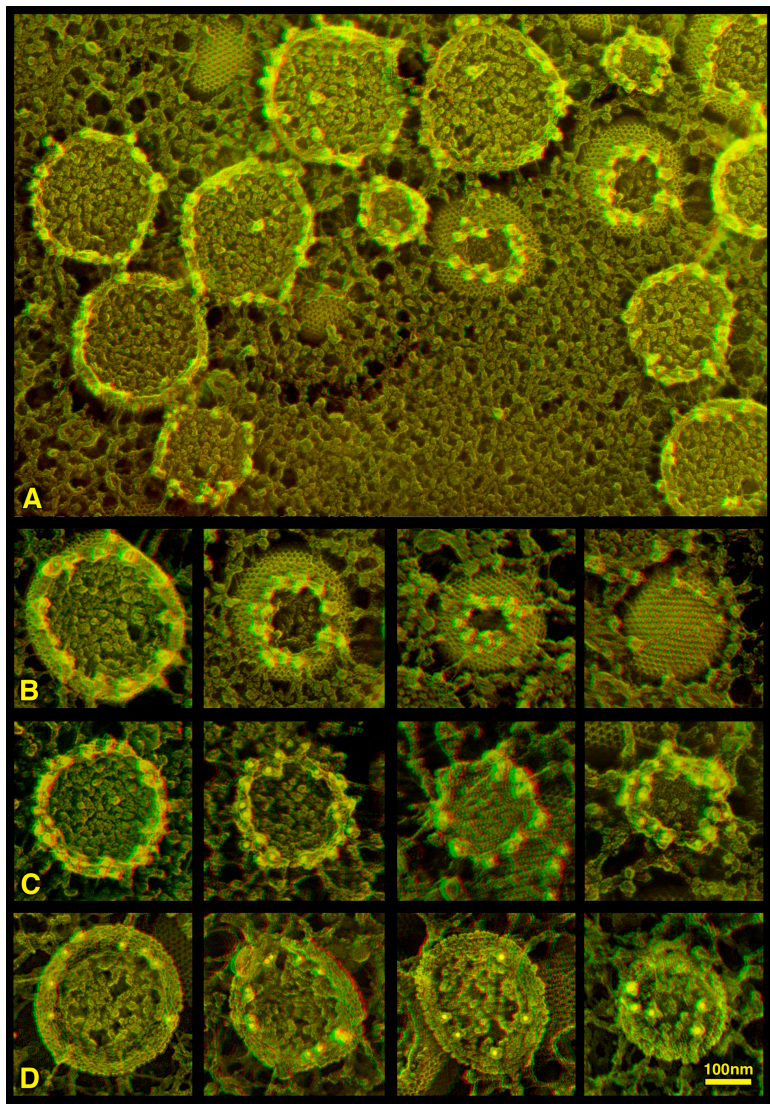


**Figure 2. 3-D deep-etch EM images of immunogold-labeled IVs.** Thawed cryosections of cells infected with VACV were labeled as described in Fig. 1 except that the antibody was to a V5 epitope at the NH<sub>2</sub> terminus of D13 (A–C) or to a COOH-terminal epitope of A17 (D) and was processed for deep-etch EM. (A) Typical overview of immunodecorated IVs. (B–D) Selected IVs that were uncut or cut at various depths off their equator. Gold particles that decorate the IVs, which normally appear electron dense, here look white as a result of the contrast reversal involved in producing anaglyph 3-D images.

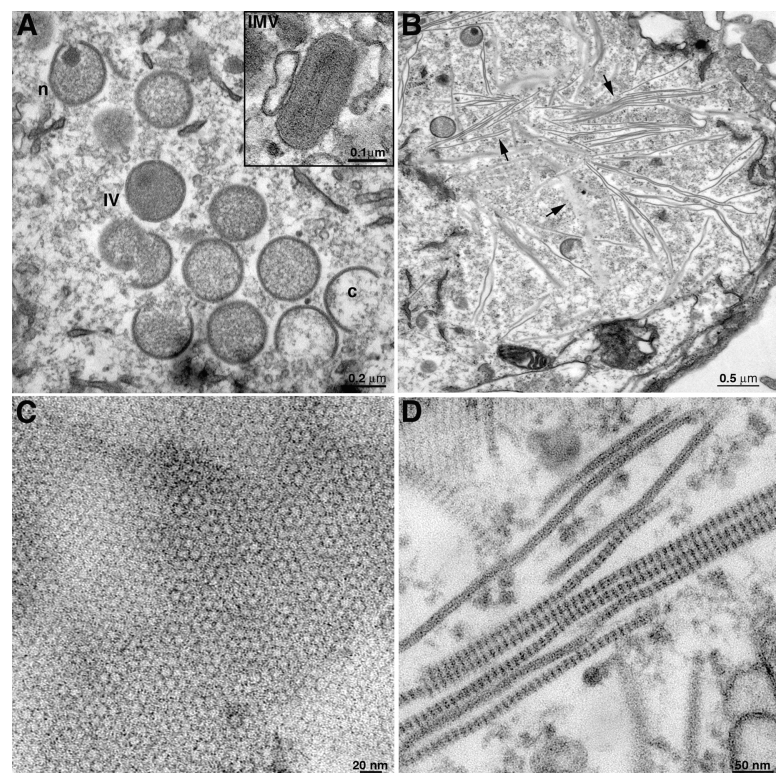
Deep-etch EM was also used to reevaluate the location of the COOH terminus of the A17 membrane protein, which had been mapped to the concave surface of IV by conventional immunogold labeling (Krijnse-Locker et al., 1996; Wolffe et al., 1996). This technique revealed that gold labeling of A17 was also largely restricted to the cut surfaces of IVs (Fig. 2 D). Nevertheless, close comparisons (Fig. 2, antibody to D13 in C vs. antibody to A17 in D) revealed that A17 labeling was slightly internal to that of D13. This same pattern of A17 immunogold labeling was also obtained with antibodies to the NH<sub>2</sub> terminus of A17 (not depicted).

The deep-etch EM results indicated that the ambiguities of traditional immuno-EM analyses of D13 are caused by the exclusive labeling of IV cut surfaces, which is confounded by the image superimposition that is inherent in nonstereoscopic viewing of thin sections. Nevertheless, because all such immunolabeling is indirect and, thus, limited in resolution to ~15–20 nm, the present finding that anti-D13 antibodies decorate only the cut edges of IVs does not prove that D13 forms the honeycomb lattice itself. The next series of experiments, however, established that D13 does form this external scaffold.

#### Mutated D13 forms flat lattice sheets that are unassociated with membranes

Previous studies demonstrated that expression of the D13 protein is necessary to form the external scaffold of IVs (Zhang and Moss, 1992; Sodeik et al., 1994). We show that a mutated form of D13 forms lattice structures with altered properties and that synthesis of other viral late proteins is not required to form this lattice. Several years ago, while carrying out EM experiments involving the simultaneous transfection of multiple VACV genes, our NIH laboratory (unpublished data) noted that the expression of one cloned D13L gene caused the formation of unusual inclusions in the cytoplasm of transfected cells. This effect was traced to a mutation that occurred during PCR copying and cloning of the D13L ORF. The mutation was shown to be an A to G transition at nucleotide 1538, causing a predicted aspartic acid to glycine change at amino acid 513. At that time, we were not yet thinking that D13 might form honeycomb structures on the surface of IVs, but given the new information, we decided to follow up this EM observation to determine whether the unusual structures that were formed by D13<sup>D513G</sup> were indeed comprised of honeycomb lattice elements.

**Figure 3. Transmission EM of lattice sheets formed by mutated D13<sup>D513G</sup>.** Cells were infected with vR0-65K in the absence of inducer and were transfected with a plasmid expressing wild-type D13 (A) or D13<sup>D513G</sup> (B–D). The cells were fixed, embedded in Epon, and viewed by transmission EM. Crescents (c), IVs, an IV with a nucleoid (n), and an IMV (inset) are shown in A. Arrows in B point to unusual structures; occasional crescents and IV are also seen. At higher magnification, the unusual structures in B appear as lattice sheets en face in C and as side views in D. Note the Moiré patterns in C, which were caused by the layering of lattice sheets.



To do this, we took advantage of a conditional lethal D13L-null mutant called vR0-65K, which requires an inducer for D13 expression and formation of crescents and IVs (Zhang and Moss, 1992). By withholding inducer from cells infected with vR0-65K, we could repress endogenous D13, selectively express various forms of D13 from transfected plasmids, and determine whether they complement the defect in vR0-65K or form aberrant structures in infected cells. As anticipated, the transfection of a plasmid encoding wild-type D13 fully complemented vR0-65K's genetic defect and yielded many normal IVs and IMVs (Fig. 3 A). In contrast, transfection with the plasmid encoding D13<sup>D513G</sup> yielded viral factories that were filled with numerous abnormal structures as well as a few crescents and IVs that resulted from incomplete repression of the endogenous D13L gene of vR0-65K (Fig. 3 B). At higher magnification, it was evident that the abnormal structures consisted of broadly extended hexagonal lattices that frequently layered upon one another to yield complex Moiré patterns when cut en face (Fig. 3 C) or consisted of images of striated ribbons when cut transversely (Fig. 3 D). Inclusions that were surrounded by irregular membranes lacking the lattice coat and resembling those formed in the absence of D13 or in the presence of rifampicin were also seen (not depicted). Thus, the D13<sup>D513G</sup> point mutation caused the protein to polymerize into flat, purely hexagonal sheets instead of the curved hexagonal/pentagonal coats that are normally seen on the surface of IV membranes.

Deep-etch EM was used to further characterize the unusual hexagonal lattices that are generated by D13<sup>D513G</sup>. This technique yielded strict surface views of the lattices, thereby avoiding the Moiré patterns that were generated by the overlap of adjacent sheets in thin sections (Fig. 4, A and B), and

showed that the size of hexagons in flat sheets matched the size of hexagons in the normal honeycombs on IVs (Fig. 4 A, compare the sheet with the IV in the inset). Specifically, both forms of lattice display a 6–7-nm vertex-to-vertex spacing within their hexagons. They differ only in that the aberrant flat sheets contain seemingly endless numbers of these hexagons without interruption, whereas normal honeycombs on IVs are each composed of a limited number of hexagons (1,400–1,500). These are mixed with 300–400 lattice variations that consist of pentagons or heptagons (unpublished data). The strict regularity of the flat sheets permitted straightforward computer averaging of their projected images (Fig. 4 C). In this study, this was performed by manual algorithms of translation and superimposition in Photoshop either while the image was maintained in three dimensions or after it was reduced to two dimensions as described in Creating image averages...operations. The latter flattening to a two-dimensional (2-D) image allowed us to apply  $\pm 60^\circ$  rotational averaging as well as translational averaging to the images, which revealed even more clearly that each hexagon is formed by six globular subunits that were 6–7 nm in diameter (Fig. 4 C, right gray panel). This conclusion was consistent with the finding of point defects, which represent missing 6–7-nm globular subunits, in many of the 3-D surface replicas (Fig. 4 B) and will be further substantiated when describing D13 trimers (see Fig. 9).

#### Viral proteins, in addition to D13, are not required to form lattice sheets

The protein components of crescents and IVs, including D13 (Weinrich et al., 1985), are expressed only after genome replication because their genes are regulated by late stage promoters.

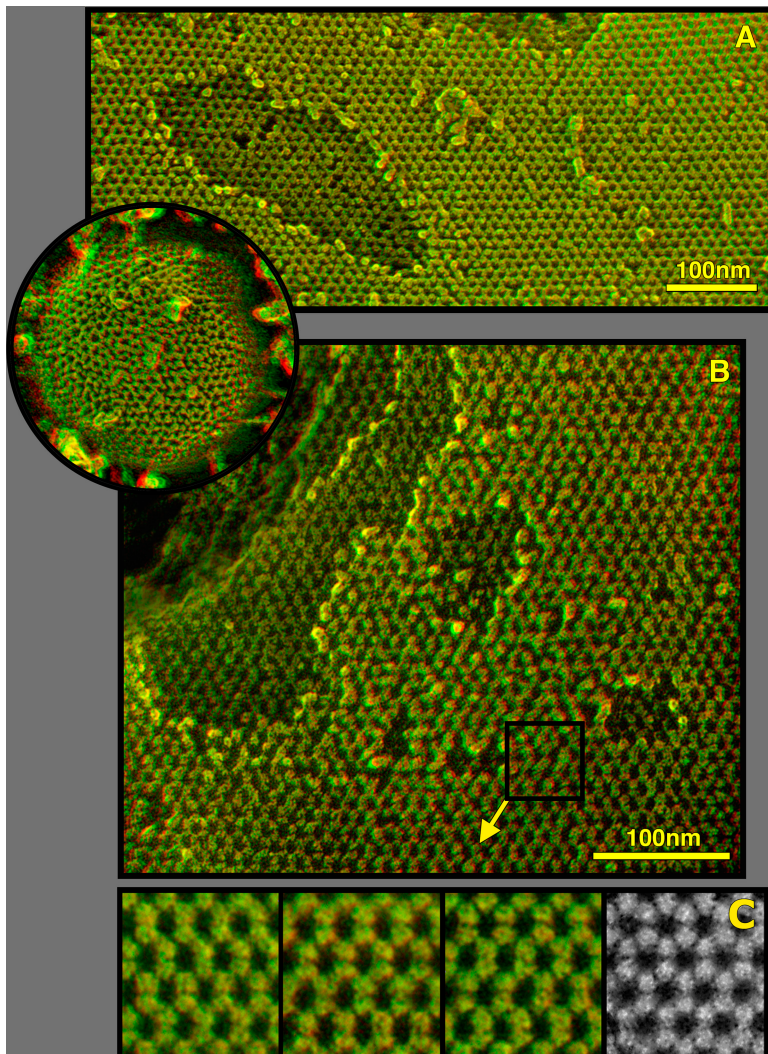


**Figure 4. Deep-etch EM image of  $D13^{D513G}$  sheets.** (A) Comparison of a stack of flat sheets formed as in Fig. 3 with the surface honeycomb of a spherical IV from a wild-type infection (inset), both at the same magnification. The pentagons present in the curved honeycomb of IV are absent from the perfectly hexagonal lattices of  $D13^{D513G}$  sheets. (B) Higher magnification of a stack of  $D13^{D513G}$  sheets that have been freeze fractured to show subjacent layers in the top left. The surface sheet shows lattice and packing defects that suggest the globular elements at each vertex tend to pair or twin (vertically in this particular view). This pairing tendency was also seen in purified D13 oligomers (compare with Fig. 9). Several of the more ordered regions of the D13 lattice (of a size indicated by the black square above the arrow) were subjected to image enhancement and are shown in C in three dimensions (left three panels) and two dimensions (right). Image enhancement was performed in Photoshop by horizontally and vertically translating the original three dimensions by exactly one lattice spacing (12 nm) and blending all the translated images together with the original image, giving each equal weight as described in Materials and methods. This refinement revealed more clearly that each hexagon is formed by six globular subunits.

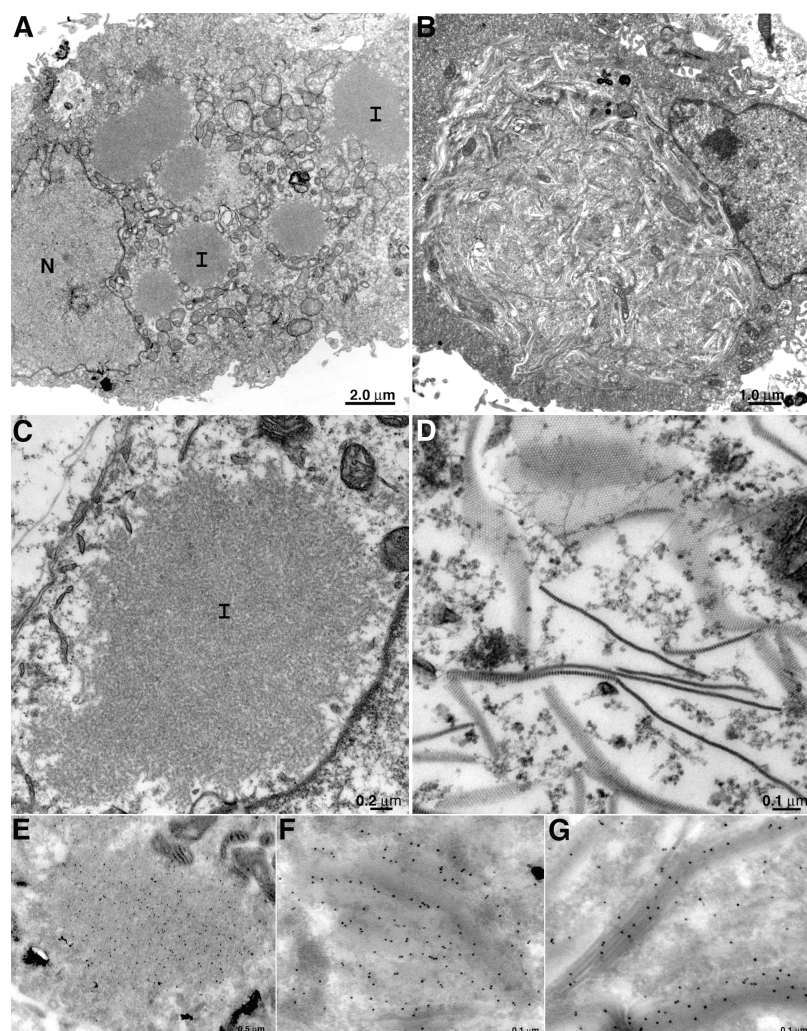
We took advantage of this fact to design further experiments to determine whether other viral late proteins, in addition to D13, are needed to form a honeycomb lattice. We constructed plasmids containing either the wild-type D13 gene or  $D13^{D513G}$  under control of a bacteriophage T7 promoter and transfected them into cells that were infected with a recombinant VACV expressing bacteriophage T7 RNA polymerase (Fuerst et al., 1987). The presence of cytosine arabinoside prevented expression of the endogenous D13 gene as well as all other late genes. Transmission EM of cells that were transfected with a plasmid expressing wild-type D13 showed masses of electron-dense material (Fig. 5, A and C), which resembled inclusions of D13 that were observed in cells infected with VACV in the presence of rifampicin (Sodeik et al., 1994). No hexagonal lattices were ever observed in these cells, indicating that wild-type D13 has no tendency to form lattice structures in the absence of IV membranes. In contrast, the cells were filled with honeycomb lattices when  $D13^{D513G}$  was expressed (Fig. 5, B and D). These  $D13^{D513G}$  sheets, which were clearly formed in the absence of other viral late proteins, were also visualized by deep-etch EM and were found to be identical to those shown in Fig. 4.

Immunogold labeling with anti-D13 antibody confirmed that the granular inclusions formed by wild-type D13 (Fig. 5 E) and the sheets formed by  $D13^{D513G}$  (Fig. 5, F and G) in the presence of cytosine arabinoside did, indeed, contain the D13 protein. Moreover, deep-etch EM showed that the immunogold labeling of D13 occurred exclusively at the cut edges of flat lattice sheets (Fig. 6), exactly as was observed with curved lattices on IV (Fig. 2). In addition, the latter mode of 3-D viewing showed that even when the sheets were layered against each other or stacked up into thicker multilayers, there was no sign of intercalated lipid membranes (Fig. 4, A and B; and Fig. 6).

#### D13 forms trimers

Viral capsid proteins are frequently homotrimeric (Benson et al., 2004), as would be expected from the geometric perspective that continuous hexagonal lattices are built out of an expanded series of trimeric vertices (Buckminster Fuller and Applewhite, 1975). Thus, we sought to determine whether the D13 protein also forms homotrimers. We produced vHisD13, which is a recombinant VACV encoding six histidine residues immediately after the start codon of the D13L ORF, in order to

**Figure 5. Visualization and immunogold labeling of honeycomb lattice sheets formed by D13<sup>D513G</sup> in the absence of other viral late proteins.** Cells were infected with VACV in the presence of AraC and were transfected with a plasmid encoding wild-type D13 (A, C, and E) or D13<sup>D513G</sup> (B, D, F, and G). The cells were fixed, embedded in Epon (A–D), or thawed cryosections were stained with antibody to the COOH-terminal D13 peptide followed by protein A gold (E–G) and were viewed by transmission EM. (A and C) Inclusions of D13 protein (I) at low and high magnification, respectively. N, nucleus. (B and D) En face and side views of lattice sheets at low and high magnification. Inclusions are immunogold labeled in E, and lattice sheets are immunogold labeled in F and G. Note that the magnification in F and G is higher than in E.



purify the protein by affinity chromatography. The recombinant virus replicated well, indicating that the tag did not affect the function of the essential D13 protein. Recombinant D13 was affinity purified from extracts of infected cells and was an-

alyzed by SDS-PAGE and Coomassie blue staining. A major polypeptide migrating at the predicted mass of ~62.7 kD was resolved (Fig. 7 A). The identity of the HisD13 protein was confirmed by Western blotting using anti-D13 peptide anti-

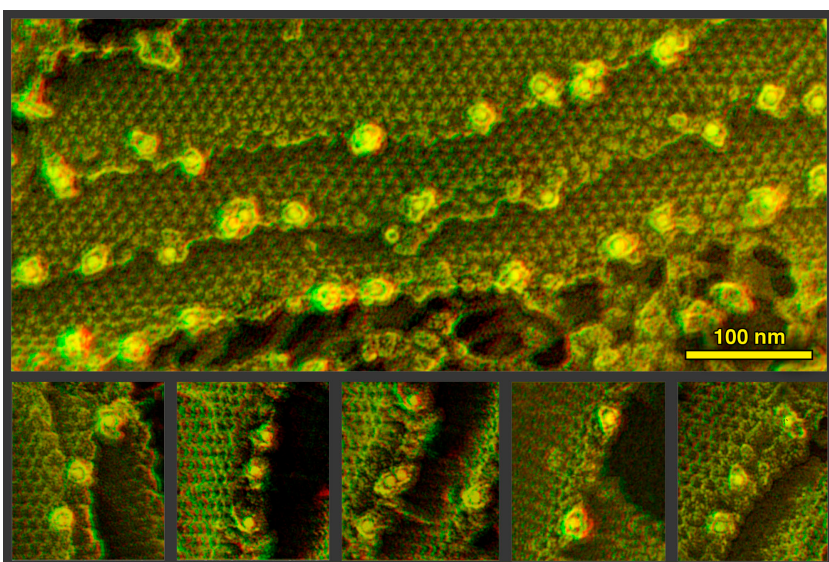


**Figure 6. 3-D deep-etch EM of immunogold-labeled honeycomb lattice sheets formed by D13<sup>D513G</sup>.** Samples were prepared and imaged as described in Fig. 2. Again, gold particles decorating the cut edges of sheets appear white in these 3-D anaglyphs. Bottom insets present optimal edge views of cryosectioned and gold-decorated sheets.

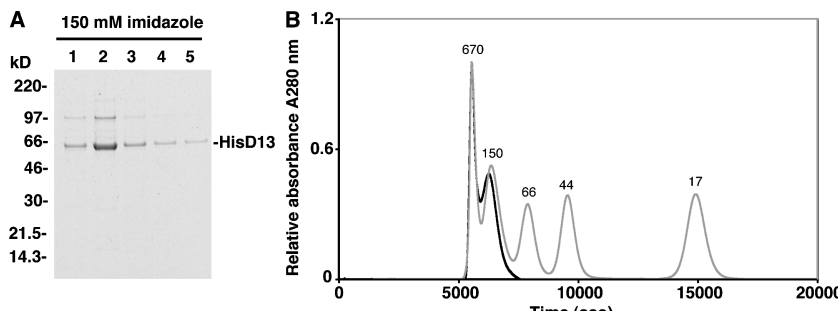


**Figure 7. SDS-PAGE and gel filtration of affinity-purified HisD13.** (A) HisD13 was purified by Talon metal affinity chromatography from the cytoplasm of cells infected with vHisD13. Proteins from consecutive fractions (1–5) that eluted with 150 mM imidazole were resolved by SDS-PAGE and were stained with Coomassie blue. The masses in kD of protein markers are indicated on the left. The major band was identified as D13 by Western blotting (not depicted); the weaker top band is a contaminant. (B) Affinity-purified undenatured HisD13 was applied to a Sephadex G-200 gel filtration column, and the protein elution profile was determined from absorbance at 280 nm. The elution of marker proteins is shown in gray and their masses in kD are indicated.

body (not depicted). When purified, undenatured HisD13 was passed through a Sephadex G-200 gel filtration column, two major peaks were detected (Fig. 7 B). The first peak eluted in the void volume of the column, whereas the second eluted slightly faster than a 150-kD protein marker, which is consistent with the expected 188-kD mass of a D13 trimer. Peaks corresponding to dimers and monomers were not found.

Nondenaturing PAGE was used to obtain a more accurate measure of the mass of native HisD13 based on the method of Ferguson (1964). By comparing the mobility of purified, undenatured HisD13 with the mobilities of proteins of known mass in gels of different polyacrylamide concentrations, a value of  $192.7 \pm 2.7$  kD (indicative of a stoichiometry of 3.1) was determined (Fig. 8 A). Addition of the affinity tag and the purification procedure had no effect on multimerization. This was determined by native gel electrophoresis followed by Western blotting of D13 protein from unpurified cytoplasmic extracts of cells that were infected with either vHisD13 or standard VACV (not depicted).

Ideally, sedimentation equilibrium would offer the best analytical ultracentrifuge approach for the determination of molar mass because this methodology is independent of shape considerations. An attempt was made to determine the molar mass of D13 using sedimentation equilibrium, but it was unsuccessful because of time-dependent aggregation over the 2–3 d of the experiment. Instead, boundary sedimentation velocity was used to further analyze the protein species in fresh affinity-purified HisD13 samples. The major protein peak had an  $s$  value of 7.65 S. Correcting for the effects of density and viscosity of the buffer solution, an  $s_{20,w}$  of 8.39 S was obtained. The sedimentation coefficients, coupled with the weight average fitted frictional  $f/f_0$  of 1.28, allowed us to calculate the molar mass of the major peak as 169,288 (Fig. 8 B), which gave a stoichiometry of 2.70 for HisD13. As described in Characterization of D13...velocity, D13 could be modeled as an oblate ellipsoid with a diameter of 14.77 nm and a short radial axis of 2.83 nm. Additional minor peaks of 11 and 3.7 S were also detected by sedimentation (Fig. 8 B). The fast component could

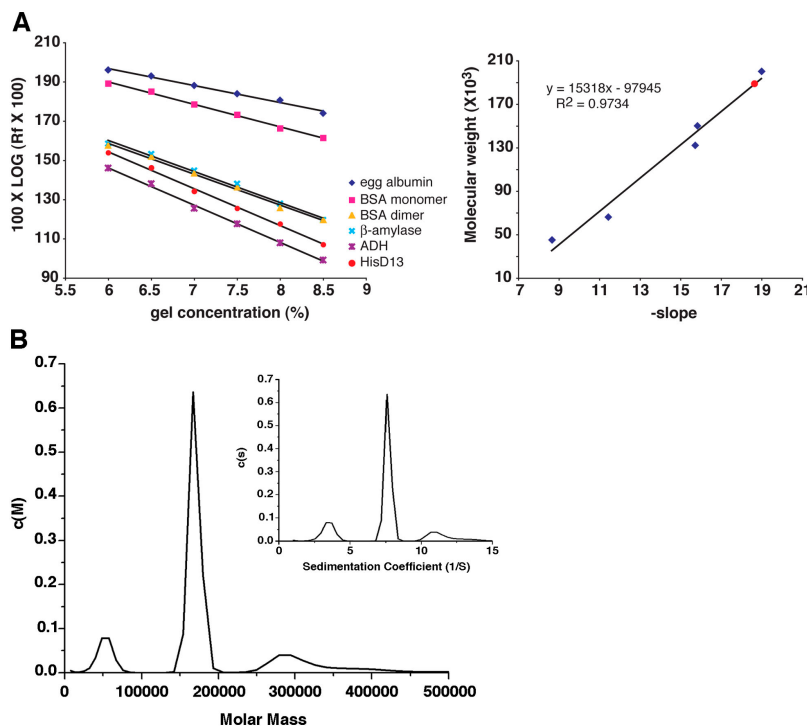


**Figure 8. Oligomeric state of native HisD13.** (A) Affinity-purified HisD13 was analyzed by electrophoresis in a series of nondenaturing polyacrylamide gels as described in Materials and methods. (left) Relative mobilities of HisD13 and marker proteins versus polyacrylamide gel concentration. Marker proteins are color coded. Rf, relative migration distance. (right) Masses of the proteins are plotted versus slopes of the lines from the right panel, and the mass of HisD13 is interpolated (red). (B) Molar mass or sedimentation coefficient distributions were obtained from the boundary sedimentation velocity data (not depicted) of the D13 sample by the computational analysis described in Materials and methods. The molar mass distribution  $c(M)$  versus  $M$  was calculated from the  $c(s)$  versus  $s$  distribution, which is shown in the inset. The differential distribution  $c(M)$  is in units of absorbance per molar mass multiplied by 100,000, and  $c(s)$  is in units of absorbance per Svedberg.

be a dimer of the D13 trimeric structure, but the slow one did not appear to fit a monomeric state of D13.

#### EM of affinity-purified HisD13

Gel filtration analysis indicated that a portion of the D13 that was purified by affinity chromatography eluted in the void volume (Fig. 7 B), suggesting the presence of protein aggregates or high order multimers. To visualize these structures by EM, material that eluted directly from the metal affinity column without a gel filtration step was adsorbed to mica flakes and was prepared for molecular imaging by deep-etch EM. This primarily yielded images of individual ~9-nm globules (Fig. 9, second row). These globules presumably represented platinum-coated D13 trimers (~9 nm was expected for a 6–7-nm globule coated with 2–3 nm of platinum). The globules looked very similar in size and shape to individual components in the rifampicin-induced D13 inclusions that deep-etch EM resolved *in situ* (Fig. 9, first row). Additionally, the purified globules were found in pairs and higher multimers (Fig. 9, third and fourth rows) as well as in larger oligomers displaying a honeycomb-like pattern (Fig. 9, fifth and sixth rows). As expected, the honeycomb fragments on mica displayed the same 6–7-nm vertex-to-vertex lattice spacing as the broad, flat sheets observed *in situ* in cells expressing D13<sup>DS13G</sup> (Fig. 9, seventh and eighth rows).

## Discussion

The absence of an icosahedral protein shell distinguishes mature, brick-shaped poxvirus virions from the capsid-coated spherical virions of other double-stranded DNA viruses. Nevertheless, a honeycomb lattice resembling virion capsids does coat the surface membrane of poxviruses when they are immature spheres but is discarded during subsequent steps of morphogenesis (Heuser, 2005). By combining microscopic, genetic, and biochemical studies, we demonstrated that trimers of the poxvirus D13 protein form the unit structure of this transitory honeycomb lattice. This conclusion fits well with previous data, including evidence that the external membrane scaffold does not form when the expression of D13 is repressed (Zhang and Moss, 1992). However, in order to definitively conclude that D13 does indeed form the external scaffold, we had to explain previous immunogold labeling studies that depicted D13 as lining the concave surface of IMV (Sodeik et al., 1994; Vanslyke and Hruby, 1994). By applying deep-etch EM techniques to visualize immunogold-labeled IV in three dimensions, we found that ambiguities in the traditional immuno-EM analysis of D13 resulted from image superimposition that was inherent in nonstereoscopic viewing of thin sections. Furthermore, we found that honeycomb lattice fragments were present in affinity-purified D13 preparations, and these had the same geometric parameters as the honeycombs on IVs that were analyzed *in situ*. Also, we obtained evidence that D13 is trimeric based on gel filtration, native gel electrophoresis, and sedimentation analysis of the soluble protein. This finding is important because geometric considerations require that all continuous hexagonal lattices be constructed of trimeric elements posi-

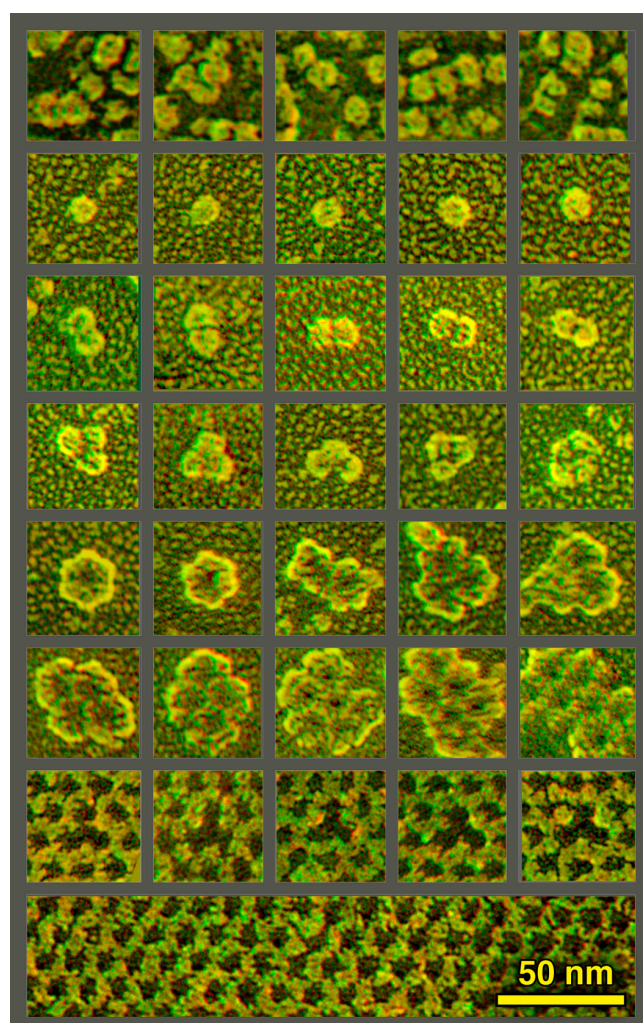


**Figure 9. Deep-etch EM of D13 multimers and fragments isolated by affinity chromatography.** The affinity-purified protein was applied to mica flakes for deep-etch EM (second to sixth rows) and was compared at the same magnification with the entities of D13 inclusion bodies in rifampicin-treated cells (first row) and with D13<sup>DS13G</sup> sheets in transfected cells (seventh and eighth rows). The single globules presumed to be trimers of D13 (second row) should be compared with the point defects that are often found in *in situ* hexagonal sheets (seventh row), such as those in Fig. 4 B. The tendency for D13 globules to twin (third row) reflects the same tendency seen *in situ* in Fig. 4 B. Note that even though the platinum coating was heavier in the fifth and sixth rows compared with the seventh and eighth rows, the lattice parameters are similar.

tioned at the vertices of each facet (Buckminster Fuller and Apblewhite, 1975). Indeed, the capsids of numerous viruses have been shown to be composed of homotrimers (Benson et al., 2004; Flint et al., 2004).

During a normal VACV infection, the D13 lattice forms a 10–15-nm-thick layer that is closely apposed to the lipoprotein membrane of crescent and IV membranes. This association occurs concomitantly with viral membrane formation so that nascent viral membranes always appear to be coated over their entirety. Uncoated viral membranes form, however, when the expression of D13 is repressed (Zhang and Moss, 1992) or when the reversible inhibitor rifampicin is present (Moss et al., 1969). In the latter case, D13 is distant from viral membranes

and accumulates in the cell in large inclusions. In this study, deep-etch EM has shown that these inclusions are composed of globule masses the size of D13 trimers. Thus, it becomes of interest to determine whether rifampicin prevents the association of D13 trimers with each other or whether it prevents their association with the nascent viral membrane. The normal tight association of the honeycomb with the viral membrane is presumably mediated by protein–protein interactions. Preliminary coimmunoprecipitation experiments indicated an association of D13 with IV membrane proteins (unpublished data), and this is now being followed up. The mechanism(s) involved in removal of the D13 scaffold during viral maturation at the time when the spherical IV is transformed into the brick-shaped IMV represents another avenue for further investigation. Deep-etch EM has caught this stage occasionally but has not yet yielded images that suggest the mechanism.

The coating of IV membranes with D13 did not occur when the codon for D13 amino acid 513 was mutated from aspartic acid to glycine. The consequence of the mutation, however, was quite different from that induced by rifampicin, which causes the D13 trimers to accumulate in depots. Instead, the mutated D13 protein formed sheets resembling the honeycomb lattice of IVs except that they were completely flat, were composed exclusively of hexagons, and formed multilayers that showed no evidence of any membrane affinity. These sheets formed even when the synthesis of all other viral late proteins was prevented. The propensity of the D13<sup>D513G</sup> protein to form apparently pure protein sheets could be explained either by a weaker interaction with membrane proteins or by an enhanced self association that preempts its interaction with membranes. IVs are fragile, transient viral forms and, thus far, have not been successfully purified for either biochemical or structural studies. Our finding that D13<sup>D513G</sup> forms flat lattices in the absence of other viral late proteins opens the possibility that such sheets could be reassembled in vitro from purified soluble trimers for high resolution analysis, as has been previously performed for mature VACV particles (Cyrklaff et al., 2005).

Iyer et al. (2001) pointed out that a domain of D13 has homology with certain capsid proteins, notably those of asfarviruses, iridoviruses, and phycodnaviruses, which they suggested are evolutionarily related to poxviruses. The atomic structure of a phycodnavirus capsid protein indicates that it exists as a trimer, each monomer of which has a “jelly roll” fold (Nandhagopal et al., 2002). This structural feature is found in the capsids of other viruses such as bacteriophage PRD1 and adenovirus (Abrescia et al., 2004). Sequence similarities of asfarvirus and iridovirus capsid proteins predict a similar structural feature near the COOH terminus (Iyer et al., 2001; Benson et al., 2004). In poxvirus D13 homologues, however, this domain was replaced by an unrelated sequence that is not predicted to form a jelly roll-type structure. Presumably, this divergence occurred during the evolution of poxviruses away from some ancestor that did have an icosahedral capsid surrounding a lipid membrane. Thus, the retention of a capsidlike scaffold around the immature form of poxviruses suggests that their morphogenesis, like embryogenesis, may reflect aspects of the historical sequence of their evolution.

## Materials and methods

### Cells and viruses

Wild-type and recombinant VACVs were propagated in BS-C-1 and HeLa cells as previously described (Earl et al., 1998a) except for vR0-65K, which was grown in the presence of 50 µM IPTG (Zhang and Moss, 1992).

### Construction of recombinant viruses

Standard procedures were used to construct and isolate recombinant viruses (Earl et al., 1998b). Both vHisD13 and vV5D13 viruses were constructed by transient dominant selection (Falkner and Moss, 1990) except that GFP and neomycin were used as markers. Plaques that contained recombinant VACVs expressing GFP were picked with the aid of an inverted fluorescence microscope (model DM IRB; Leica) and were clonally purified by repeated plaque isolations. DNA sequences encoding a V5 (GKPIPN-PLGLDST) or six-histidine epitope tag were added immediately after the first methionine codon of the D13L ORF endogenous copy of wild-type VACV strain Western Reserve. PCR and DNA sequencing confirmed the genetic alterations of recombinant viruses.

### Transmission EM of immunogold-labeled thawed cryosections

VACV-infected cells were washed, fixed with 4% PFA/0.05% glutaraldehyde, injected with 2.3 M sucrose, quick frozen, and cut into 70-nm sections. Cryosections were picked up on grids, thawed, washed free of sucrose, and stained with antibody to the COOH-terminal 15-mer D13 peptide (Sodeik et al., 1994) or the COOH-terminal 12-mer A17 peptide (Wolffe et al., 1996). Then, cryosections were stained with protein A conjugated to 10-nm gold spheres (G. Postuma, University Medical Center Utrecht, Utrecht, Netherlands) or with a mouse mAb to a V5 epitope tag (Invitrogen) followed by rabbit anti-mouse IgG (Cappel-ICN Pharmaceuticals) and were again stained with protein A conjugated to 10-nm gold spheres. Sections were analyzed on a transmission electron microscope (model Philips CM100; FEI Co.) essentially as described previously (Griffiths et al., 1983; Tokuyasu, 1986).

### Deep-etch EM of immunogold-decorated cryosections

Cryosections of ~100 nm thick were prepared as described above and were picked up on 3 × 3-mm glass coverslips that had been coated with a thin film of carbon and glow discharged just before use. The coverslips were processed and immunogold labeled as described above, after which they were placed in 2% glutaraldehyde fixative and transferred to the Washington University School of Medicine for deep-etch EM. Subsequently, they were washed free of fixative with several changes of water, quick frozen with a liquid helium-cooled copper block “slammer” (the standard Heuser Cryopress; Heuser et al., 1979), mounted in a Balzers vacuum evaporator, and completely freeze dried by warming to –100°C for 15 min. Finally, the samples were replicated by an electron beam application of 2–4 nm of platinum as they rotated in the vacuum (Heuser and Salpeter, 1979). The replicas were released from coverslips by a brief flotation on concentrated hydrofluoric acid (the need for this step explains why the coverslips were coated with carbon in the first place; if they were not, the hydrofluoric acid would contact the gold in the replica directly and dissolve it away). Replicas of such gold-decorated cryosections were viewed with a standard transmission electron microscope (model 100 CX; JEOL) that was operated at 100 kV and were recorded at two different degrees of tilt ( $\pm 10^\circ$ ) on standard EM film. Thereafter, the stereo pairs of film were aligned by superimposition on a copy stand and were rerecorded as 4,492 × 3,328 pixel (17 Mp) images with a digital single lens reflex camera (model EOS-1Ds Mark II; Canon). Finally, the digital image pairs were converted (one to red and the other to green) and were layered on top of each other with the screen blending mode in Adobe Photoshop to create the final 3-D anaglyphs that are shown in this study (Heuser, 2000).

### Creating image averages using standard Adobe Photoshop operations

Steps that were taken to enhance images in Fig. 4 (C) by using Photoshop (Adobe Systems) are listed as follows: (1) Copy the original image and paste the copy on top of the original image as a superimposed new layer. (2) In Photoshop’s layer → layer style → blending options, convert the fill opacity of the new layer from 100 to 50% to make it semitransparent and reveal the original image underneath. (3) Using Photoshop’s edit → free transform command, translate the new layer exactly one lattice spacing sideways until the two layers look by eye to be perfectly in register. (4) Temporarily turn off the new layer’s visibility in Photoshop’s window → layers → visibility menu and repeat steps 1–4 with another new copy of

the original image, only this time translating it two lattice spacings laterally before registering it by eye. (5) Also temporarily turn off this new layer's visibility and repeat steps 1–4 with yet another copy of the original image, only this time translating it three lattice spacings laterally before registering it. (6) Keep making original copies and repeating steps 1–5, translating in step 3 in any lattice direction deemed suitable (in the averaged 3-D images presented in Fig. 4 C, this was repeated a total of 10 times, translating in both horizontal and vertical directions because the original lattice was intentionally perfectly oriented horizontally to begin with). (7) Turn the visibility of all layers back on in Photoshop's window → layers → visibility menu, and the final averaged image will become visible. (8) Flatten the image by collapsing all layers together in Photoshop's layers → flatten image menu, and the computer-averaged image is ready for cropping and sizing.

#### Deep-etch EM of transfected and infected cells

VACV-infected and -transfected cells were fixed with 2% glutaraldehyde in 70 mM NaCl, 30 mM Hepes buffer, pH 7.4, and 2 mM CaCl<sub>2</sub>, scraped from their culture dishes, and sent as suspensions in fixative to the Washington University School of Medicine for further processing. There, they were pelleted, washed free of glutaraldehyde with the fixative vehicle, and were finally quick frozen, freeze fractured, deep etched, and rotary replicated with platinum by the standard technique (Heuser, 2005). The resultant replicas were viewed and worked up exactly as described above for cryosections.

#### Deep-etch EM of macromolecules that were adsorbed to mica flakes

This was accomplished as previously described (Heuser, 1989, 2000). In brief, two drops of a suspension of finely ground mica flakes were added to 0.5 ml of a solution containing the D13 protein at ~20 µg/ml, and the protein was allowed to adsorb to the mica for ~30 s. The mica flakes were pelleted by gentle centrifugation and washed twice with a solution containing 70 mM KCl, 30 mM Hepes, pH 7.2, 5 mM MgCl<sub>2</sub>, and 3 mM EGTA. Then, they were layered onto a thin slice of aldehyde-fixed lung for support during quick freezing, as described in the previous section. The frozen slurry of mica flakes was freeze fractured in a standard Balzer's freeze-etch machine and was immediately etched for 3 min at -100°C. It was then rotary replicated with ~2 nm of platinum that was applied from an angle of 11° above the horizontal and backed with an ~10-nm film of pure carbon. Replicas were separated from the mica by overnight flotation on a solution of concentrated hydrofluoric acid and were finally washed several times in water before being picked up on 75 mesh formvar-coated microscope grids, which were viewed and processed as described in the previous section.

#### Affinity purification and gel filtration of HisD13

HeLa S3 cells were infected with vHisD13 for 24 h and were lysed with 50 mM Na phosphate buffer, pH 7.0, 0.3 M NaCl, and 0.5% NP-40. The soluble extract was incubated with Talon resin (CLONTECH Laboratories, Inc.) for 3 h at 4°C, and the resin was washed with 50 mM Na phosphate, 0.3 M NaCl, and 5 mM imidazole. The bound HisD13 protein was eluted with 0.15 M imidazole in 50 mM sodium phosphate buffer and 0.3 M NaCl. Gel filtration was on a 16 × 60-cm column of Sephadryl S200 HR (GE Healthcare) that was equilibrated with 0.3 M NaCl and 0.1 M Na phosphate, pH 7.0, with a flow rate of 0.5 ml per minute. Fractions were monitored by absorbance at 280 nm.

#### Determination of the mass of native HisD13 by PAGE

Affinity-purified HisD13 was analyzed by using the method adapted from Ferguson (1964), Davis (1964), and Bryan (1977) as described in Sigma Technical Bulletin No. MKR-137.

#### Characterization of D13 by sedimentation velocity

Boundary sedimentation velocity measurements were made in an analytical ultracentrifuge (model Optima XLi; Beckman-Coulter). Analysis was performed at 20°C at a rotor speed of 35,000 rpm. The centrifuge cell was filled with 0.4 ml of protein solution at a concentration of 0.40 mg/ml. Absorbance scans were obtained at 280 nm. Sedimentation coefficient distribution analysis to deconvolute the boundary velocity data into sedimenting species was performed as described previously (Schuck, 2000) using the public domain software Sedfit (<http://www.analyticalultracentrifugation.com/>). Hydrodynamic analysis of the data was performed using the software Sednterp (<http://www.bbri.org/RASMB/rasmb.html>). Sednterp was also used to determine the partial specific volume of D13 and the viscosity ( $\eta$ ) and density ( $\rho$ ) for the buffer/salt solution that was used in sedimentation analyses.

We thank the members of the Laboratory of Viral Diseases (NIAID) for their many suggestions and particularly Norman Cooper for assistance with cell culture. In addition, we thank the members of the Heuser laboratory for a superb effort, especially Mrs. Robyn Roth for EM.

This research was supported, in part, by the Intramural Research Program of NIAID (NIH). The deep-etch EM work in this study was supported by U.S. Public Health Service grant GM29647 to J. Heuser.

Submitted: 6 April 2005

Accepted: 3 August 2005

## References

- Abrescia, N.G., J.J. Cockburn, J.M. Grimes, G.C. Sutton, J.M. Diprose, S.J. Butcher, S.D. Fuller, C. San Martin, R.M. Burnett, D.I. Stuart, et al. 2004. Insights into assembly from structural analysis of bacteriophage PRD1. *Nature*. 432:68–74.
- Baldick, C.J., and B. Moss. 1987. Resistance of vaccinia virus to rifampicin conferred by a single nucleotide substitution near the predicted NH<sub>2</sub> terminus of a gene encoding an M, 62,000 polypeptide. *Virology*. 156:138–145.
- Benson, S.D., J.K. Bamford, D.H. Bamford, and R.M. Burnett. 2004. Does common architecture reveal a viral lineage spanning all three domains of life? *Mol. Cell*. 16:673–685.
- Bryan, J.K. 1977. Molecular weights of protein multimers from polyacrylamide gel electrophoresis. *Anal. Biochem*. 78:513–519.
- Buckminster Fuller, R., and E.J. Applewhite. 1975. Synergetics: Explorations in the Geometry of Thinking. Charles Scribner's Sons, New York. 876 pp.
- Cyrklaff, M., C. Risco, J.J. Fernandez, M.V. Jimenez, M. Esteban, W. Baumeister, and J.L. Carrascosa. 2005. Cryo-electron tomography of vaccinia virus. *Proc. Natl. Acad. Sci. USA*. 102:2772–2777.
- Dales, S., and L. Siminovitch. 1961. The development of vaccinia virus in Earle's L strain cells as examined by electron microscopy. *J. Biophys. Biochem. Cytol*. 10:475–503.
- Dales, S., V. Milovanovitch, B.G.T. Pogo, S.B. Weintraub, T. Huima, S. Wilton, and G. McFadden. 1978. Biogenesis of vaccinia: isolation of conditional lethal mutants and electron microscopic characterization of their phenotypically expressed defects. *Virology*. 84:403–428.
- Davis, B.J. 1964. Disc electrophoresis. II. Method and application to human serum proteins. *Ann. NY Acad. Sci.* 121:404–427.
- de Harven, E., and D.S. Yohn. 1966. The fine structure of monkey tumor poxvirus. *Cancer Res.* 26:995–1008.
- Earl, P.L., N. Cooper, S. Wyatt, B. Moss, and M.W. Carroll. 1998a. Preparation of cell cultures and vaccinia virus stocks. In *Current Protocols in Molecular Biology*. Vol. 2. F.M. Ausubel, R. Brent, R.E. Kingston, D.D. Moore, J.G. Seidman, J.A. Smith, and K. Struhl, editors. John Wiley & Sons Inc., New York. 16.16.1–16.16.3.
- Earl, P.L., B. Moss, L.S. Wyatt, and M.W. Carroll. 1998b. Generation of recombinant vaccinia viruses. In *Current Protocols in Molecular Biology*. Vol. 2. F.M. Ausubel, R. Brent, R.E. Kingston, D.D. Moore, J.G. Seidman, J.A. Smith, and K. Struhl, editors. Greene Publishing Associates & Wiley Interscience, New York. 16.17.1–16.17.19.
- Essani, K., R. Dugre, and S. Dales. 1982. Biogenesis of vaccinia: involvement of spicules of the envelope during virion assembly examined by means of conditional lethal mutants and serology. *Virology*. 118:279–292.
- Falkner, F.G., and B. Moss. 1990. Transient dominant selection of recombinant vaccinia viruses. *J. Virol.* 64:3108–3111.
- Ferguson, K.A. 1964. Starch-gel electrophoresis—application to the classification of pituitary proteins and polypeptides. *Metabolism*. 13:985–1002.
- Flint, S.J., L.W. Enquist, V.R. Racaniello, and A.M. Skalka. 2004. Principles of Virology. ASM Press, Washington, D.C. 918 pp.
- Fuerst, T.R., P.L. Earl, and B. Moss. 1987. Use of a hybrid vaccinia virus T7 RNA polymerase system for expression of target genes. *Mol. Cell. Biol.* 7:2538–2544.
- Griffiths, G., K. Simons, G. Warren, and K.T. Tokuyasu. 1983. Immunoelectron microscopy using thin, frozen sections: application to studies of the intracellular transport of Semliki Forest virus spike glycoproteins. *Methods Enzymol.* 96:466–485.
- Grimley, P.M., E.N. Rosenblum, S.J. Mims, and B. Moss. 1970. Interruption by rifampicin of an early stage in vaccinia virus morphogenesis: accumulation of membranes which are precursors of virus envelopes. *J. Virol.* 6:519–533.
- Heuser, J. 1989. Protocol for 3-D visualization of molecules on mica via the quick-freeze, deep-etch technique. *J. Electron Microsc. Tech.* 13:244–263.
- Heuser, J. 2005. Deep-etch EM reveals that the early poxvirus envelope is a single membrane bilayer stabilized by a geodetic “honeycomb” surface coat.

- J. Cell Biol.* 169:269–283.
- Heuser, J.E. 2000. Membrane traffic in anaglyph stereo. *Traffic*. 1:35–37.
- Heuser, J.E., and S.R. Salpeter. 1979. Organization of acetylcholine receptors in quick-frozen, deep-etched, and rotary-replicated Torpedo postsynaptic membrane. *J. Cell Biol.* 82:150–173.
- Heuser, J.E., T.S. Reese, M.J. Dennis, Y. Jan, L. Jan, and L. Evans. 1979. Synaptic vesicle exocytosis captured by quick freezing and correlated with quantal transmitter release. *J. Cell Biol.* 81:275–300.
- Iyer, L.M., L. Aravind, and E.V. Koonin. 2001. Common origin of four diverse families of large eukaryotic DNA viruses. *J. Virol.* 75:11720–11734.
- Krijnse-Locker, J., S. Schleich, D. Rodriguez, B. Goud, E.J. Snijder, and G. Griffiths. 1996. The role of a 21-kDa viral membrane protein in the assembly of vaccinia virus from the intermediate compartment. *J. Biol. Chem.* 271:14950–14958.
- Miner, J.N., and D.E. Hruby. 1989. Rifampicin prevents virosome localization of L65, an essential vaccinia virus polypeptide. *Virology*. 170:227–237.
- Mohandas, A.R., and S. Dales. 1995. Involvement of spicules in the formation of vaccinia virus envelopes elucidated by a conditional lethal mutant. *Virology*. 214:494–502.
- Moss, B. 2001. Poxviridae: the viruses and their replication. In *Fields Virology*, vol. 2. D.M. Knipe and P.M. Howley, editors. Lippincott Williams & Wilkins, Philadelphia, PA. 2849–2883.
- Moss, B., E.N. Rosenblum, E. Katz, and P.M. Grimley. 1969. Rifampicin: a specific inhibitor of vaccinia virus assembly. *Nature*. 224:1280–1284.
- Nagaya, A., B.G. Pogo, and S. Dales. 1970. Biogenesis of vaccinia: separation of early stages from maturation by means of rifampicin. *Virology*. 40:1039–1051.
- Nandhagopal, N., A.A. Simpson, J.R. Gurnon, X. Yan, T.S. Baker, M.V. Graves, J.L. Van Etten, and M.G. Rossmann. 2002. The structure and evolution of the major capsid protein of a large, lipid-containing DNA virus. *Proc. Natl. Acad. Sci. USA*. 99:14758–14763.
- Schuck, P. 2000. Size-distribution analysis of macromolecules by sedimentation velocity ultracentrifugation and lamm equation modeling. *Biophys. J.* 78:1606–1619.
- Sodeik, B., G. Griffiths, M. Ericsson, B. Moss, and R.W. Doms. 1994. Assembly of vaccinia virus: effects of rifampin on the intracellular distribution of viral protein p65. *J. Virol.* 68:1103–1114.
- Tartaglia, J., A. Piccini, and E. Paoletti. 1986. Vaccinia virus rifampicin-resistance locus specifies a late 63,000 Da gene product. *Virology*. 150:45–54.
- Tokuyasu, K.T. 1986. Application of cryoultramicrotomy to immunocytochemistry. *J. Microsc.* 143:139–149.
- Vanslyke, J.K., and D.E. Hruby. 1994. Immunolocalization of vaccinia virus structural proteins during virion formation. *Virology*. 198:624–635.
- Weinrich, S.L., E.G. Niles, and D.E. Hruby. 1985. Transcriptional and translational analysis of the vaccinia virus late gene L65. *J. Virol.* 55:450–457.
- Wolffe, E.J., D.M. Moore, P.J. Peters, and B. Moss. 1996. Vaccinia virus A17L open reading frame encodes an essential component of nascent viral membranes that is required to initiate morphogenesis. *J. Virol.* 70:2797–2808.
- Zhang, Y., and B. Moss. 1992. Immature viral envelope formation is interrupted at the same stage by lac operator-mediated repression of the vaccinia virus D13L gene and by the drug rifampicin. *Virology*. 187:643–653.